

# Construction of $\text{Bi}_2\text{S}_3/\text{TiO}_2/\text{MoS}_2$ S-Scheme Heterostructure with a Switchable Charge Migration Pathway for Selective $\text{CO}_2$ Reduction

Khaled Alkanad, Abdo Hezam, Qasem Ahmed Drmash, Sujay Shekar Ganganakatte Chandrashekar, Abeer A. AlObaid, Ismail Warad, Mohammed Abdullah Bajiri, and Lokanath Neratur Krishnappagowda\*

Switching between the redox potential of an appropriate semiconductor heterostructure could show critical applications in selective  $\text{CO}_2$  reduction. Designing a semiconductor photocatalyst with a wavelength-dependent response is an effective strategy for regulating the direction of electron flow and tuning the redox potential. Herein, the switching mechanism between two charge migration pathways and redox potentials in a  $\text{Bi}_2\text{S}_3/\text{TiO}_2/\text{MoS}_2$  heterostructure by regulating the light wavelength is achieved. In situ irradiated X-ray photoelectron spectroscopy (ISI-XPS), electron spin resonance (ESR), photoluminescence (PL), and experimental scavenger analyses prove that the charge transport follows the S-scheme approach under UV–vis–NIR irradiation and the heterojunction approach under vis–NIR irradiation, confirming the switchable feature of the  $\text{Bi}_2\text{S}_3/\text{TiO}_2/\text{MoS}_2$  heterostructure. This switchable feature leads to the reduction of  $\text{CO}_2$  molecules to  $\text{CH}_3\text{OH}$  and  $\text{C}_2\text{H}_5\text{OH}$  under UV–vis–NIR irradiation, while  $\text{CH}_4$  and  $\text{CO}$  are produced under Vis–NIR irradiation. Interestingly, the apparent quantum efficiency of the optimal composite at  $\lambda = 600 \text{ nm}$  is 4.23%. This research work presents an opportunity to develop photocatalysts with switchable charge transport and selective  $\text{CO}_2$  reduction.

## 1. Introduction

Despite ongoing attempts to minimize the emission of  $\text{CO}_2$  since the Industrial Revolution,  $\text{CO}_2$  emissions continue to increase at a higher rate. Consequently, climate change has already affected human health, water supplies, agriculture, and the biodiversity of the oceans and soil.<sup>[1]</sup> Photocatalytic  $\text{CO}_2$  reduction is a multi-functional strategy, which not only reduces the emission of  $\text{CO}_2$ , but also transfers it to usable fuels such as methane ( $\text{CH}_4$ ), carbon monoxide ( $\text{CO}$ ), ethanol ( $\text{C}_2\text{H}_5\text{OH}$ ), formaldehyde ( $\text{HCHO}$ ), methanol ( $\text{CH}_3\text{OH}$ ), ethylene ( $\text{C}_2\text{H}_2$ ), and formic acid ( $\text{HCOOH}$ ), based on the number of reductions in the electrons and their redox potential.<sup>[2–5]</sup> Therefore, efficient photocatalytic  $\text{CO}_2$  reduction is measured by the electronic structure of the photocatalyst and its light absorption and the redox

potential of exciting charges.<sup>[4–6]</sup> Therefore, an excellent photocatalyst should feature broad light absorption, proper heterojunction interfacial contact, a low electron/hole recombination rate, high charge transport, an appropriate redox potential, and  $\text{CO}_2$

K. Alkanad, S. S. Ganganakatte Chandrashekar,  
L. Neratur Krishnappagowda  
Department of Studies in Physics  
University of Mysore  
Manasagangotri, Mysuru 570 006, India  
E-mail: lokanath@physics.uni-mysore.ac.in


A. Hezam  
Department of Physics  
Faculty of Science  
Ibb University  
70270 Ibb, Yemen

Q. A. Drmash  
Interdisciplinary Research Center for Hydrogen and Energy Storage  
King Fahd University of Petroleum and Minerals  
Dhahran 31261, Saudi Arabia

A. A. AlObaid  
Department of Chemistry  
College of Science  
King Saud University  
P.O. Box 245, Riyadh 11451, Saudi Arabia

I. Warad  
Department of Chemistry and Earth Sciences  
Qatar University  
2713 Doha, Qatar

M. A. Bajiri  
Department of Studies and Research in Industrial Chemistry  
School of Chemical Sciences  
Kuvempu University  
Shankaraghatta 577 451, India

 The ORCID identification number(s) for the author(s) of this article can be found under <https://doi.org/10.1002/solr.202100501>.

DOI: 10.1002/solr.202100501

product selectivity.<sup>[7–11]</sup> Particularly, for an effective reduction reaction, the heterostructure should have a proper conduction band minimum (CBM) potential, which should be higher than the potential of the selective reduction product.

Although many promising photocatalysts for CO<sub>2</sub> reduction have been fabricated, they suffer from poor light harvesting, high recombination rate of electrons/holes, weak redox potential, and poor product selectivity or the requirement of a sacrificial agent, which massively restrict achievable practical uses. Semiconducting metal oxide and sulfide photocatalysts were regarded as the most efficient approaches among the other methods of CO<sub>2</sub> reduction.<sup>[6,12–14]</sup> TiO<sub>2</sub> is a typical semiconductor photocatalyst that can be formed in three different crystal phases: anatase, rutile, and brookite,<sup>[4,15]</sup> where the anatase phase has been frequently used for CO<sub>2</sub> reduction due to its stability and morphological calibration.<sup>[16–20]</sup> The large bandgap of TiO<sub>2</sub> limits the absorbance of the full light spectrum because it absorbs only light in the UV region. Therefore, TiO<sub>2</sub>-based photocatalysts with different molecular surface morphologies play an important role in determining surface adsorption capacities and surface charge separation.<sup>[21]</sup> MoS<sub>2</sub> and Bi<sub>2</sub>S<sub>3</sub> are considered desirable catalysts or cocatalysts in the photocatalytic system due to their morphology tuning and low bandgaps, which improve their light harvesting, optical properties, and charge mechanism transfer.<sup>[13,22–29]</sup>

Multidimensional structure architecture results in a higher surface area and optimal interfacial interaction of semiconducting photocatalysts, contributing to higher photocatalytic efficiency by accelerating electron and hole transportation, and impeding their recombination.<sup>[11,24,30–32]</sup> The conversion of CO<sub>2</sub> to a specific product is highly desirable for energy conversion. However, the CO<sub>2</sub> conversion product depends primarily on the CB redox potential of the accumulated electrons.<sup>[10,23,25,33,34]</sup> Consequently, the regulation of the charge carriers can tune the redox potential and strongly affects the photocatalytic activity of the heterostructure.

In van der Waal heterostructures, Z-scheme and heterojunction systems are two well-known charge migration pathways for efficient heterostructure photocatalysts.<sup>[35,36]</sup> However, the direct Z-scheme photocatalytic mechanism has been gradually replaced by a new step-scheme (S-scheme) heterojunction mechanism to solve the high recombination rates of photogenerated electron-hole pairs in the Z-scheme system and their low reduction and oxidation abilities in type-II heterojunction photocatalysts.<sup>[8,31,37,38]</sup> Initially, the proposed S-scheme heterojunction stated that the two selected semiconductors constructing the S-scheme photocatalyst must be n-type semiconductors.<sup>[37,38]</sup> Recent investigations indicate that the S-scheme heterojunction is also constituted of n-type and p-type semiconductors.<sup>[39–42]</sup> Nevertheless, it is challenging to construct S-scheme or type-II heterojunctions for a specific target. Various factors need to be optimized to attain the ideal junction system, such as the dispersion of the coupling semiconductors, and the nature of contact at the interface. Heterostructure materials of S-scheme charge migration have gained remarkable research attention as they facilitate the separation of the free carriers, expand the spectral response to the visible range, and optimize the redox potential.<sup>[8,31,37–44]</sup> Recent studies reported that regulation of the electron flow could be achieved by selecting the proper

synthesis method,<sup>[35,36,45]</sup> selecting the proper type of coupled semiconductors,<sup>[41]</sup> and varying the nature of the interface contact through the creation of vacancies,<sup>[9]</sup> an ultrathin layered heterojunction,<sup>[31]</sup> or by the electrostatic self-assembly method.<sup>[46]</sup>

In this research work, we used the wavelength of irradiated light to regulate the charge transfer pathway. A Bi<sub>2</sub>S<sub>3</sub>/TiO<sub>2</sub>/MoS<sub>2</sub> heterostructure was prepared by a microwave hydrothermal method and it exhibits excellent photocatalytic efficiency toward CO<sub>2</sub> reduction. The prepared heterostructure showed a switchability of the charge transfer with different wavelengths of irradiation light. Under UV-vis-NIR, all the electrons in the valence band (VB) of TiO<sub>2</sub>, Bi<sub>2</sub>S<sub>3</sub>, and MoS<sub>2</sub> can be excited to the conduction band (CB), generating an internal electrical field from TiO<sub>2</sub> to Bi<sub>2</sub>S<sub>3</sub> and MoS<sub>2</sub>. The experimental result revealed that under UV-vis-NIR, the binding energy of TiO<sub>2</sub> experiences a slight positive shift, whereas the Bi<sub>2</sub>S<sub>3</sub> and MoS<sub>2</sub> binding energies show a negative shift, implying the migration pathway of charge carrier follows the S-scheme system, whereas under vis-NIR only, the electrons in the VB of Bi<sub>2</sub>S<sub>3</sub> and MoS<sub>2</sub> can be excited to the CB, resulting in a positive shift of their binding energies and a slight negative shift of the binding energy of TiO<sub>2</sub>, indicating a form of type II heterojunction system. Interestingly, the tuning of the composite junction results in switching between the accumulated charge carriers' redox potentials, which promotes the CO<sub>2</sub> reduction selectivity.

## 2. Results and Discussion

### 2.1. Structural Studies

The crystallites of TiO<sub>2</sub>, MoS<sub>2</sub>, Bi<sub>2</sub>S<sub>3</sub>, MoS<sub>2</sub>/Bi<sub>2</sub>S<sub>3</sub> (BTM0), and Bi<sub>2</sub>S<sub>3</sub>/TiO<sub>2</sub>/MoS<sub>2</sub> (BTM1.5) were investigated by a powder X-ray diffractometer (PXRD), as shown in **Figure 1**. All the diffraction peaks of the pristine TiO<sub>2</sub> are indexed to the (101), (103), (004),

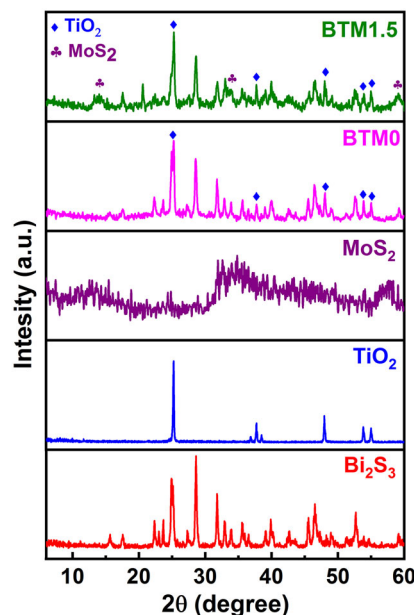


**Figure 1.** PXRD pattern for Bi<sub>2</sub>S<sub>3</sub>, TiO<sub>2</sub>, MoS<sub>2</sub>, BTM0, and BTM1.5 samples.

(112), (200), (105), and (211) planes, which revealed that  $\text{TiO}_2$  has an anatase phase (JCPDS 21-1272), the sharpness in the peaks indicating the excellent crystallinity of the  $\text{TiO}_2$ . For the pristine  $\text{MoS}_2$ , all X-ray diffraction (XRD) patterns are well indexed to the hexagonal phase of  $\text{MoS}_2$  with diffraction peaks assigned to (002), (100), (105), and (110) planes (JCPDS 37-1492).<sup>[47]</sup> The XRD patterns of the pure  $\text{Bi}_2\text{S}_3$  are indexed to the (020), (120), (220), (101), (310), (021), (211), (221), (410), (311), (240), (231), (041), (141), (421), (002), (431), (160), (222), (351), (161), and (242) planes of the orthorhombic  $\text{Bi}_2\text{S}_3$  structure (JCPDS 00-017-0320). The XRD pattern for the binary BTM0 sample revealed the composite formation. Most of the diffraction peaks of  $\text{TiO}_2$  and  $\text{Bi}_2\text{S}_3$  were detected with some overlapping for some peaks, revealing the good dispersion of  $\text{TiO}_2$  among  $\text{Bi}_2\text{S}_3$ . In the ternary BTM1.5 composite, the XRD pattern consists of all  $\text{TiO}_2$ ,  $\text{Bi}_2\text{S}_3$ , and  $\text{MoS}_2$  diffraction peaks that confirm the composite formation. This suggests that  $\text{Bi}_2\text{S}_3$  nanorods and  $\text{TiO}_2$  nanoparticles roped with  $\text{MoS}_2$  effectively, resulting in a typical stacking of  $\text{MoS}_2$  during the growth phase.

## 2.2. Morphology Studies

Field emission scanning electron microscopy (FE-SEM) and transmission electron microscopy (TEM) analyses were used to confirm the morphology of the synthesized samples. **Figure 2a** shows a 3D flower-like structure assembled by 1D  $\text{Bi}_2\text{S}_3$  nonuniform nanorods with smooth surfaces.  $\text{MoS}_2$  exhibits a 3D marigold flower-like buildup of 2D-morphology nanosheets (Figure 2b). The FE-SEM image of the ternary composite exhibits the heterostructure consisting of an agglomeration of nanoparticles, nanorods, and nanosheets. The established  $\text{Bi}_2\text{S}_3/\text{TiO}_2/\text{MoS}_2$  heterostructure acquired three different phases, nanorods, nanosheets, in addition to nanospheres clustered among  $\text{Bi}_2\text{S}_3$  nanorods and  $\text{MoS}_2$  nanosheets, which is attributed to  $\text{TiO}_2$  nanoparticles (Figure 2c). The interfaces between these different phases lead to large active sites to provide an excellent light response to enhance the photocatalytic properties.

The morphology of the sample BTM1.5 was elucidated by TEM (Figure 2d) to provide more insight into the crystalline structure and size distribution of the engineered ternary heterostructure.  $\text{TiO}_2$  nanoparticles' size varies between 170 and 40 nm, where the  $\text{Bi}_2\text{S}_3$  nanorods have lengths up to 590 nm and diameter around 25 nm. Figure 2f displays  $\text{TiO}_2$  nanoparticles, and  $\text{Bi}_2\text{S}_3$  nanorods are well wrapped by the  $\text{MoS}_2$  nanosheet with an intimate interfacial contact among all the phases of the heterostructure. The interfaces between the  $\text{MoS}_2$  nanosheet,  $\text{Bi}_2\text{S}_3$  nanorod, and  $\text{TiO}_2$  nanoparticles are magnified in high-resolution TEM (HR-TEM) imaging of BTM1.5. The lattice plane of a  $\text{Bi}_2\text{S}_3$  nanorod with a lattice spacing (310) is well covered with multilayers of the  $\text{MoS}_2$  nanosheet of an interlayer spacing of 0.62 nm (Figure 2e). In addition, Figure 2g displays that  $\text{MoS}_2$  multilayers of an interlayer spacing of 0.64 nm are well wrapped around the  $\text{TiO}_2$  nanoparticles. This indicates an excellent interfacial interaction among  $\text{Bi}_2\text{S}_3$ ,  $\text{TiO}_2$ , and  $\text{MoS}_2$ . Therefore, higher charge separation and large active sites lead to efficient photocatalytic performance.

## 2.3. Surface Elemental Study

X-ray photoelectron spectroscopy (XPS) was performed to investigate the composite composition and chemical state and to understand the possible charge migration pathway in the heterostructure. The survey spectrum indicates the purity of the composite, which includes only Bi, Ti, Mo, S, and O (**Figure 3a**). For much more relevant information on the chemical state of the obtained heterostructure, high-resolution XPS (HR-XPS) has been applied to Bi, Ti, Mo, S, and O core-level regions. Figure 3b shows two binding energies of 158.65 and 163.78 eV ( $\text{Bi}^{4+}$ ), demonstrating the Bi 4f core-level spectrum ascribed respectively to Bi 4f<sub>7/2</sub> and Bi 4f<sub>5/2</sub>. The peak's broadness and separation between them (5.1 eV) indicates the existence of a  $\text{Bi}^{3+}$  oxidation state in  $\text{Bi}_2\text{S}_3$ . The Gaussian fitting method was applied, and the chemical state of Bi 4f<sub>5/2</sub> was elaborated into two-component peaks with binding energies of 163.8 eV (Bi-S) and 121 eV assigned to S 2p<sub>3/2</sub>, indicating strong Bi-S bonds. The HR-XPS spectrum of Ti 2p shows two strong peaks

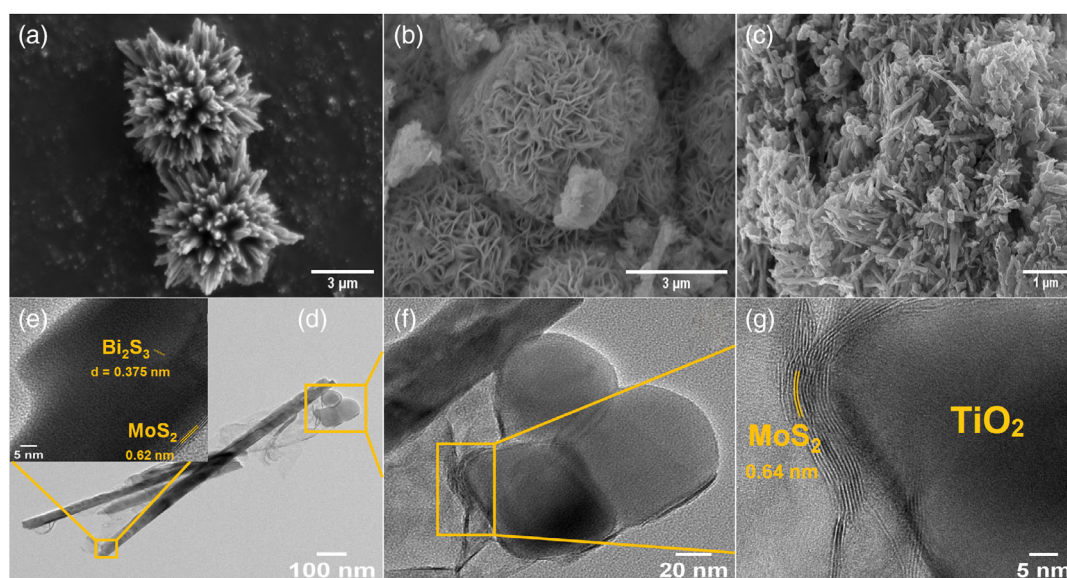


**Figure 2.** FSEM images of a)  $\text{Bi}_2\text{S}_3$ , b)  $\text{MoS}_2$ , and c) BTM1.5; d–g) TEM and HR-TEM images of BTM1.5.

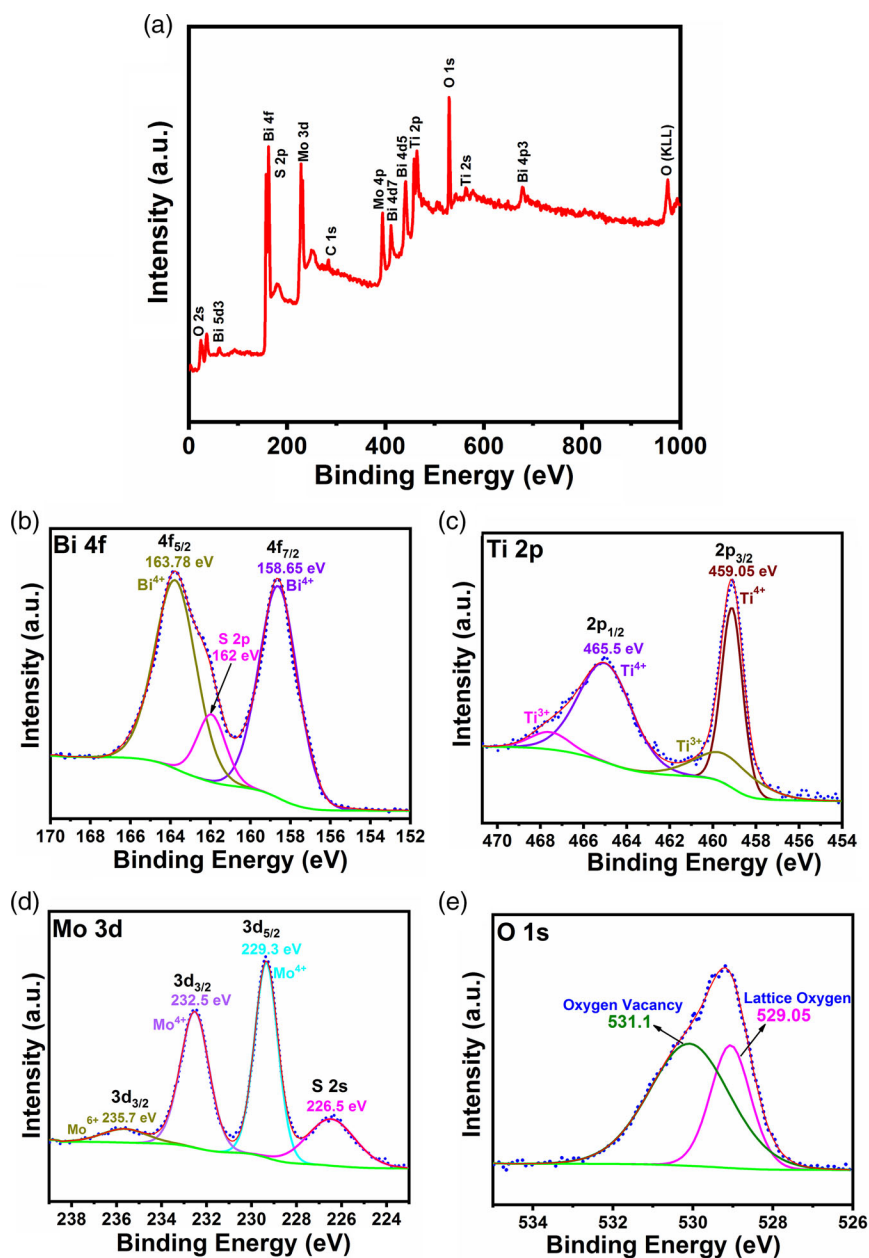


**Figure 3.** a) XPS survey spectrum of BTM1.5; HRXPS spectra of b) Bi 4f, c) Ti 2p, d) Mo 3d core level, and e) O 1s core level.

located at 459.05 and 465.05 eV, which are ascribed to Ti  $2p_{3/2}$  and Ti  $2p_{1/2}$ , respectively, arising from spin–orbit splitting. These peaks suggest the existence of Ti in the form of a  $Ti^{4+}$  state.

Using the Gaussian fitting method, two shake-up satellites located at 459.6 and 467.6 eV were observed, decreasing the area of the peak of  $Ti^{4+}$  (Figure 3c); the reduction of  $Ti^{4+}$  to the  $Ti^{3+}$  state resulting in the formation of oxygen vacancies on the surface of the composite.<sup>[48]</sup> The Mo 3d spectrum shows two intense high peaks at 229.3 and 232.5 eV arising from spin–orbit splitting of 3.2 eV, which correspond to Mo  $3d_{5/2}$  and Mo  $3d_{3/2}$ , respectively, indicating the existence of Mo in the form of the  $Mo^{4+}$  state (Figure 3d). The peak centered at 226.5 eV belongs to the S 2s

state,<sup>[49]</sup> where the peak at 235.7 eV corresponds to Mo  $3d_{3/2}$  in  $MoO_3$ , indicating that  $MoS_2$  slightly oxidized during the migration from the state of  $Mo^{4+}$  to  $Mo^{6+}$ . Such oxidation can enhance the electronic properties and produce more active sites with excellent photocatalytic efficiency.<sup>[49,50]</sup> Based on the studies mentioned earlier, the nanoheterostructure consists of  $Bi_2S_3$ ,  $TiO_2$ , and  $MoS_2$ . O 1s XPS spectra ensure the presence of oxygen vacancies on the heterostructure surface (Figure 3e). The O 1s spectrum consists of two fitted peaks observed at 529.05 and 531.1 eV ascribed respectively to the lattice oxygen and oxygen vacancies, which indicates an abundance of oxygen vacancies in the sample.



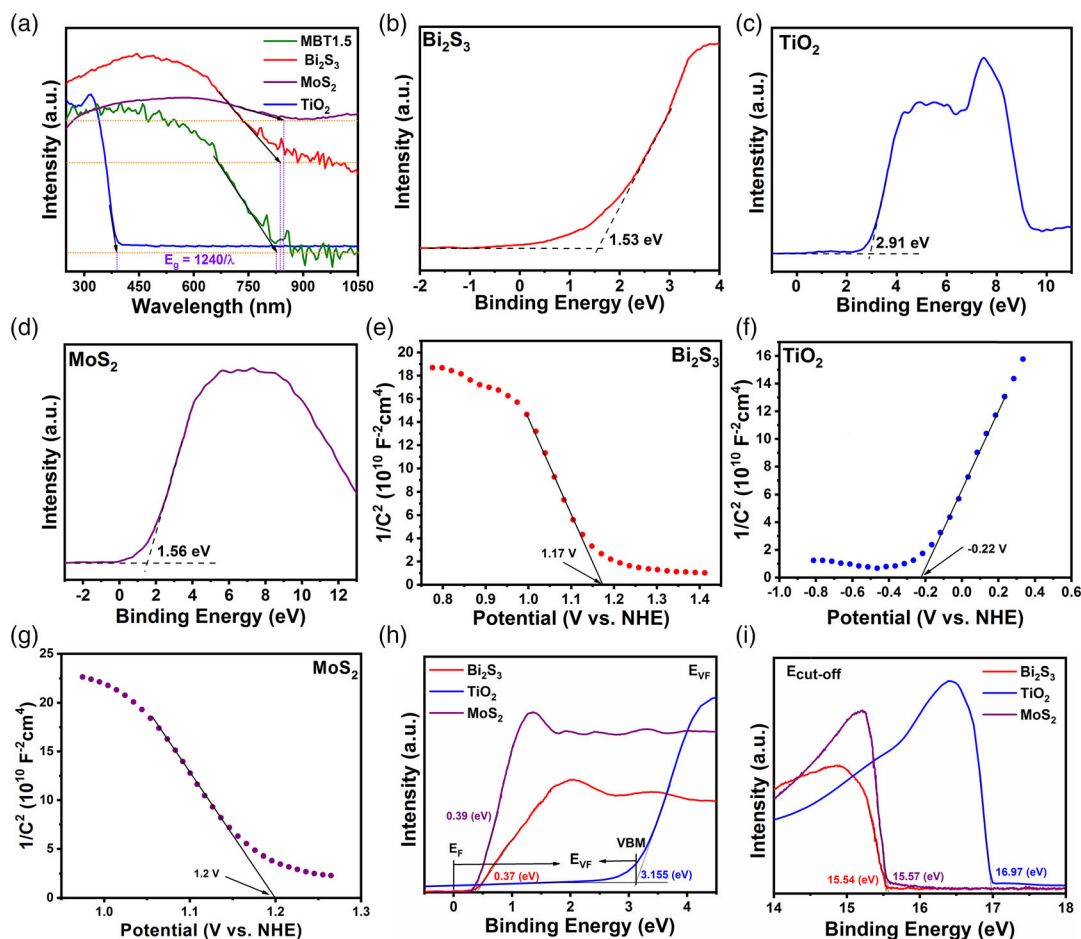


**Figure 4.** a) DRS UV-vis spectra of Bi<sub>2</sub>S<sub>3</sub>, TiO<sub>2</sub>, MoS<sub>2</sub>, and BTM1.5; VB-XPS spectra of b) Bi<sub>2</sub>S<sub>3</sub>, c) TiO<sub>2</sub>, and d) MoS<sub>2</sub>; Mott-Schottky of e) Bi<sub>2</sub>S<sub>3</sub>, f) TiO<sub>2</sub>, and g) MoS<sub>2</sub>; and h,i,j) UPS of Bi<sub>2</sub>S<sub>3</sub>, TiO<sub>2</sub>, and MoS<sub>2</sub>.

#### 2.4. Band Position Determination

A catalyst with high light absorption capability exhibits efficient photocatalytic performance and enhanced electrocatalytic property. **Figure 4a** shows UV-vis diffuse reflectance spectroscopy (UV-vis DRS) absorption spectra of pure Bi<sub>2</sub>S<sub>3</sub>, TiO<sub>2</sub>, MoS<sub>2</sub>, and ternary BTM1.5 nanoheterostructure. High light absorption is observed across the UV-vis wavelength spectrum with an absorption edge of about 838 and 846 nm for the Bi<sub>2</sub>S<sub>3</sub> nanorod and MoS<sub>2</sub> nanosheet, respectively. A significant absorption edge of about 386 nm was observed for the pure TiO<sub>2</sub> nanoparticles. The flat plot of the MoS<sub>2</sub> spectrum can be credited to the intrinsic background absorption of the black color of the MoS<sub>2</sub> nanosheet.<sup>[28]</sup> The ternary Bi<sub>2</sub>S<sub>3</sub>/TiO<sub>2</sub>/MoS<sub>2</sub> nanoheterostructure exhibits high absorption exceeding the visible light spectrum toward the NIR region with an absorption edge around 826 nm. The charge flow direction and energy gaps of Bi<sub>2</sub>S<sub>3</sub>, TiO<sub>2</sub>, and MoS<sub>2</sub> were calculated using the equation  $E_g = 1240/\lambda$ , where  $\lambda$  is the absorption edges obtained from the DRS spectra.<sup>[51]</sup> The energy gaps ( $E_g$ ) for Bi<sub>2</sub>S<sub>3</sub>, TiO<sub>2</sub>, MoS<sub>2</sub>, and the ternary Bi<sub>2</sub>S<sub>3</sub>/TiO<sub>2</sub>/MoS<sub>2</sub> nanocomposites were calculated as 1.48, 3.21, 1.46, and 1.5 eV, respectively.

The CB edge and VB edge of the pristine Bi<sub>2</sub>S<sub>3</sub>, TiO<sub>2</sub>, and MoS<sub>2</sub> were estimated using Equation (1) and (2).

$$\text{CBM} = \chi - E_{\text{ef}} - 0.5E_g \quad (1)$$

$$\text{VBM} = \text{CBM} + E_g \quad (2)$$

“CBM” is the CB minimum; “VBM” is the VB maximum of the pristine semiconductors;  $\chi$  is the semiconductor electronegativity;  $E_{\text{ef}}$  is the energy of a free electron on the hydrogen scale (about 4.5 eV); and  $E_g$  is the semiconductor bandgap energy.  $\chi$  values are 5.3, 5.8, and 5.32 eV for Bi<sub>2</sub>S<sub>3</sub>, TiO<sub>2</sub>, and MoS<sub>2</sub>, respectively.<sup>[52–54]</sup> CBM and VBM values were found to be 0.06 and 1.54 V for Bi<sub>2</sub>S<sub>3</sub>, −0.305 and 2.905 V for TiO<sub>2</sub>, and 0.09 and 1.55 V for MoS<sub>2</sub>. However, the VBM was further confirmed experimentally by valence band XPS (VB-XPS) for all the pristine semiconductors (Figure 4b–d). The VBM was calculated to be 1.53, 2.91, and 1.56 V for Bi<sub>2</sub>S<sub>3</sub>, TiO<sub>2</sub>, and MoS<sub>2</sub>, respectively, correlated with those measured by DRS UV-vis. Bi<sub>2</sub>S<sub>3</sub>, MoS<sub>2</sub>, and TiO<sub>2</sub> semiconductors’ conductivity types were determined using Mott-Schottky (M-S) measurements. The plot of M-S (1/C<sup>2</sup> versus the applied potential) was linearly fitted with the M-S equation; C is the capacitance. Figure 4e–f shows that TiO<sub>2</sub> has a positive slope, whereas

$\text{Bi}_2\text{S}_3$  and  $\text{MoS}_2$  have a negative slope, indicating that  $\text{TiO}_2$  is an n-type semiconductor, whereas  $\text{Bi}_2\text{S}_3$  and  $\text{MoS}_2$  are p-type semiconductors, which is in line with the reported literature.<sup>[17,55–58]</sup> The flat band potential determined from the X-axis intercept was found to be 1.17, –0.22, and 1.2 V versus NHE for  $\text{Bi}_2\text{S}_3$ ,  $\text{TiO}_2$ , and  $\text{MoS}_2$ , respectively. These corresponding flat bands refer to the Fermi level of the semiconductor.<sup>[59]</sup> To further confirm the energy band structure, ultraviolet photoelectron spectroscopy (UPS) measurements were conducted to determine their work functions ( $\Phi$ ) and VBM according to Equation (3)–(5).<sup>[60,61]</sup>

$$\Phi = h\nu - E_{\text{cut-off}} \text{ (vs vacuum)} \quad (3)$$

$$E_{\text{VF}} = \text{VBM} - E_{\text{F}} \text{ (vs vacuum)} \quad (4)$$

$$\text{VBM (vs NHE)} = \text{VBM (vs vacuum)} - E_{\text{ef}} \quad (5)$$

where  $h\nu = 21.22$  eV, which is the photoenergy of the monochromatic He I source;  $E_{\text{cut-off}}$  is the secondary electron cut-off edge of the samples. Figure 4i shows that  $\text{Bi}_2\text{S}_3$ ,  $\text{TiO}_2$ , and  $\text{MoS}_2$  had  $E_{\text{cut-off}}$  at 15.54, 16.97, and 15.57 eV, respectively. Considering Equation (3), the corresponding  $\Phi$  values are 5.65, 4.25, and 5.68 eV, which are the energy difference of vacuum and  $E_{\text{F}}$  for  $\text{Bi}_2\text{S}_3$ ,  $\text{TiO}_2$ , and  $\text{MoS}_2$ , respectively (Figure 5a). This indicates that  $\text{Bi}_2\text{S}_3$  and  $\text{MoS}_2$  have lower  $E_{\text{F}}$  close to their VB, where  $\text{TiO}_2$ 's  $E_{\text{F}}$  is close to its CB. These results are congruent with the earlier M–S measurements.  $E_{\text{VF}}$  is the VBM with respect to the  $E_{\text{F}}$ ; Figure 4h shows that the  $E_{\text{VF}}$  of  $\text{Bi}_2\text{S}_3$ ,  $\text{TiO}_2$ , and  $\text{MoS}_2$  was measured to be 0.37, 3.155, and 0.39 eV, respectively. The equivalent VBM (vs NHE) of  $\text{Bi}_2\text{S}_3$ ,  $\text{TiO}_2$ , and  $\text{MoS}_2$  is 1.52, 2.9, and 1.57 eV, respectively (Equation (4) and (5)), which is consistent with the previous VB–XPS and UV–DRS results.

Based on these analyses, the band structures of  $\text{Bi}_2\text{S}_3$ ,  $\text{MoS}_2$ , and  $\text{TiO}_2$  before the junction construction are shown in Figure 5a. The Fermi level of  $\text{TiO}_2$  is higher than that of  $\text{Bi}_2\text{S}_3$  and  $\text{MoS}_2$ , hence combining n-type  $\text{TiO}_2$  with p-type  $\text{Bi}_2\text{S}_3$  and  $\text{MoS}_2$  results in the formation of a nanoscale n–p heterojunction. This junction could efficiently create a sufficient

space charge layer to enhance the charge carrier transportation. The thermal equilibrium of distinct Fermi levels results in a realignment of valence and conduction bands, causing the  $\text{TiO}_2$  energy bands to move downward and those of  $\text{Bi}_2\text{S}_3$  and  $\text{MoS}_2$  to move upward. The energy band structure of BTM1.5 after junction formation is shown in Figure 5b.

## 2.5. Photocatalytic $\text{CO}_2$ Reduction

To investigate the advantage of the switchability of the electron flow for the developed material upon light sources with different wavelengths, photocatalytic  $\text{CO}_2$  reduction was performed for  $\text{Bi}_2\text{S}_3$ ,  $\text{TiO}_2$ ,  $\text{MoS}_2$ ,  $\text{Bi}_2\text{S}_3/\text{TiO}_2$ , and the  $\text{Bi}_2\text{S}_3/\text{TiO}_2$  nanocomposite with different ratios of  $\text{MoS}_2$  under UV–vis–NIR ( $\lambda = 190$ –1200 nm) and vis–NIR ( $\lambda = 400$ –1200 nm) lights for 1 h. Gas chromatography verifies that, under UV–vis–NIR, a remarkable amount of  $\text{CH}_4$  is released in the presence of pristine  $\text{TiO}_2$  nanosphere or  $\text{MoS}_2$  nanosheets (Figure 6a), whereas in the presence of pristine  $\text{Bi}_2\text{S}_3$  nanorods,  $\text{CH}_3\text{OH}$  and  $\text{C}_2\text{H}_5\text{OH}$  are produced. Compared to the pristine  $\text{Bi}_2\text{S}_3$ , the binary BTM0 and BTM1.5 enhance the reduction rate by 2.8 and 5.8 times, respectively (Figure 6a).

In contrast, no output is observed for the  $\text{TiO}_2$  nanosphere under vis–NIR, and a small amount of  $\text{CH}_4$  is produced by  $\text{MoS}_2$  nanosheets, whereas for  $\text{Bi}_2\text{S}_3$  nanorods, minor products such as  $\text{CH}_3\text{OH}$  and  $\text{C}_2\text{H}_5\text{OH}$  are detected (Figure 6b). However, the solar fuel produced by BTM0 under vis–NIR switches from  $\text{CH}_3\text{OH}$  and  $\text{C}_2\text{H}_5\text{OH}$  (under UV–vis–NIR) to  $\text{CH}_4$  and  $\text{CO}$  (Figure 6b). Moreover, the production of  $\text{CH}_4$  and  $\text{CO}$  is increased four times higher than the binary productions for BTM1.5. As a result, the charge pathway and its accumulation position varied with the applied light. Therefore, by switching from UV–vis–NIR to vis–NIR, the produced products by BTM1.5 changed from  $\text{CH}_4$  and  $\text{CO}$  to  $\text{CH}_3\text{OH}$  and  $\text{C}_2\text{H}_5\text{OH}$ . The detailed reactions and the mechanism involved are summarized subsequently. Moreover, the reactions were conducted without the catalyst and in darkness. Neither of those products was

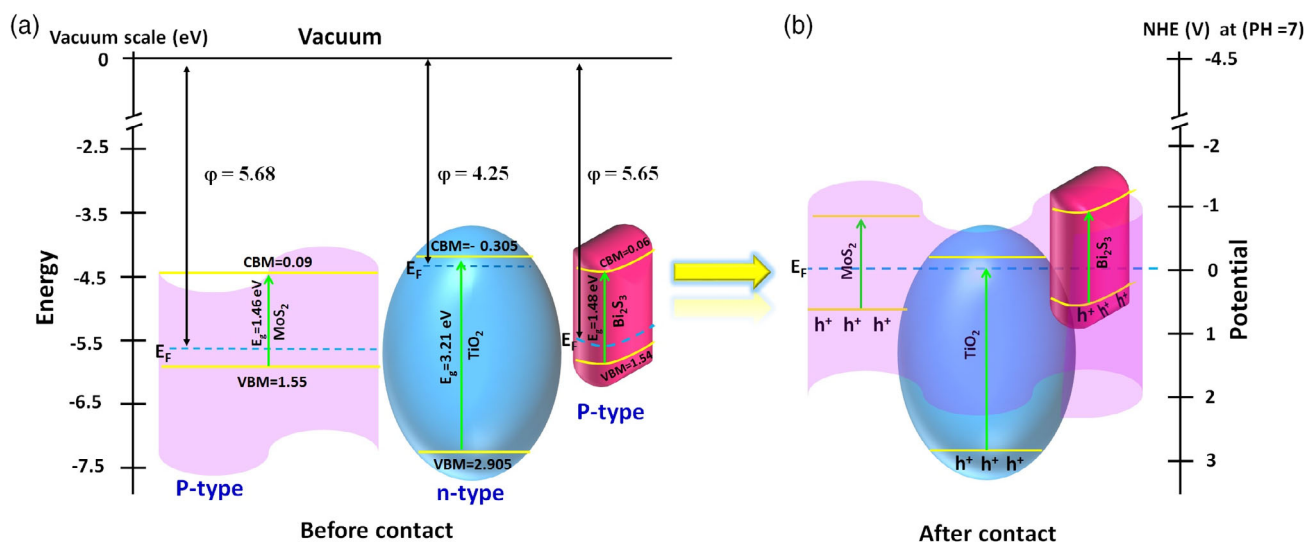


**Figure 5.** Energy band structure of  $\text{Bi}_2\text{S}_3$ ,  $\text{MoS}_2$ , and  $\text{TiO}_2$  a) before and b) after contact.

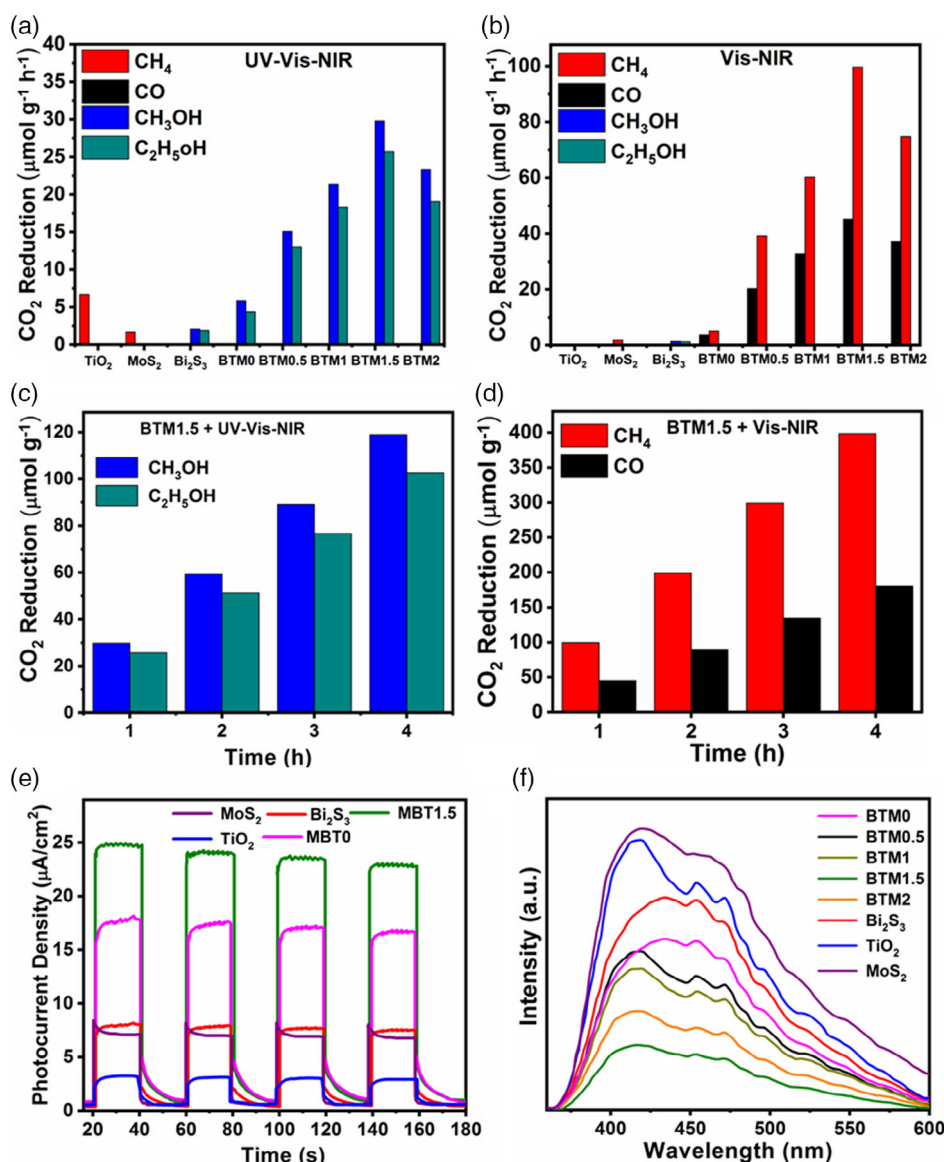


**Figure 6.** Photocatalytic CO<sub>2</sub> reduction of all the prepared photocatalysts for 1 h under a) UV-vis-NIR and b) vis-NIR irradiation; reusability and recyclability of BTM1.5 under c) UV-vis-NIR and d) vis-NIR irradiations; and e) photocurrent responses and f) photoluminescence spectra of the pristine samples and their composites.

detected, suggesting that the generated products are optimistically UV-vis-NIR/vis-NIR photocatalytic CO<sub>2</sub> reduction products.

For the optimum composite, a <sup>13</sup>C-labeled isotope experiment was conducted to ensure that the injected CO<sub>2</sub> is the only carbon source for the generated products. The reduction products of <sup>13</sup>CO<sub>2</sub> photoreduction under vis-NIR irradiation on the BTM1.5 photocatalyst can be detected in the MS spectra in Figure S1a, Supporting Information, where two indicated signals at *m/z* = 17 and 29 attributed to <sup>13</sup>CH<sub>4</sub> and <sup>13</sup>CO reduction, respectively, whereas under UV-vis-NIR irradiation, the reduction product from <sup>13</sup>CO<sub>2</sub> is seen in the MS spectra located at *m/z* = 33 for <sup>13</sup>CH<sub>3</sub>OH (Figure S1b, Supporting Information) and *m/z* = 48 for <sup>13</sup>C<sub>2</sub>H<sub>5</sub>OH (Figure S1c, Supporting Information). Additional traces of <sup>12</sup>CH<sub>3</sub>OH and <sup>12</sup>C<sub>2</sub>H<sub>5</sub>OH with

minimal intensity were detected due to their ion fragmentation. This finding demonstrates that the generated products are the result of photocatalytic reduction of CO<sub>2</sub> molecules.

Irrespective of the applied light, it can be seen from Figure 6a, b that the nanocomposites exhibit higher activity for the production of CH<sub>3</sub>OH, C<sub>2</sub>H<sub>5</sub>OH, CH<sub>4</sub>, and CO than pristine ones and the binary sample. This is due to the efficient charge transfer of photogenerated electrons and holes between the bands of the Bi<sub>2</sub>S<sub>3</sub>, TiO<sub>2</sub>, and MoS<sub>2</sub>, promoting the charge separation and inhibiting the carriers' recombination rate. Figure 6e shows that BTM1.5 gains the highest photocurrent response compared to the binary BTM0 and the pure Bi<sub>2</sub>S<sub>3</sub>, TiO<sub>2</sub>, and MoS<sub>2</sub>, demonstrating that the charge separation is highest in BTM1.5.<sup>[62]</sup> Furthermore, the photoluminescence (PL) spectrum of the

ternary BTM1.5 exhibits the lowest intensity compared to the BTM0, BTM0.5, BTM1, BTM2, Bi<sub>2</sub>S<sub>3</sub>, TiO<sub>2</sub>, and MoS<sub>2</sub> samples. This reveals that BTM1.5 has the lowest recombination rate of the charge carriers (Figure 6f).<sup>[63]</sup> However, the nanostructure's surface area and porosity play an effective role in separating and transporting charge carriers.<sup>[64]</sup> The prepared samples' Brunauer–Emmett–Teller (BET) surface area and Barrett–Joyner–Halenda (BJH) pore volume are shown in Figure S2. The samples showed porous structure, and the measured surface areas are 32 m<sup>2</sup> g<sup>−1</sup> for Bi<sub>2</sub>S<sub>3</sub>, 43 m<sup>2</sup> g<sup>−1</sup> for MoS<sub>2</sub>, 87 m<sup>2</sup> g<sup>−1</sup> for BTM0, and 142 m<sup>2</sup> g<sup>−1</sup> for BTM1.5. BTM1.5 showed an improved surface area and pore size, which account for its higher photocatalytic activity. The highest surface area, photocurrent density, and charge separation of BTM1.5 are the main factors behind the highest photocatalytic CO<sub>2</sub> reduction. It is worth mentioning that the yield of the product increases with the increase of MoS<sub>2</sub> content up to a certain amount (optimal ratio BTM1.5). On further increase in the amount of MoS<sub>2</sub>, a decrease in the yield of the produced product was observed. This might be due to the self-aggregation of MoS<sub>2</sub> in the composite and the lower rate of the interface's interaction with other contents of the composite.<sup>[7,65]</sup> In addition, the maximum yield after 4 h of reaction for BTM1.5 is 119 and 102.7 μmol g<sup>−1</sup> for CH<sub>3</sub>OH and C<sub>2</sub>H<sub>5</sub>OH, respectively, under UV–vis–NIR (Figure 6c) and 180.5 and 398.6 μmol g<sup>−1</sup> for CH<sub>4</sub> and CO, respectively, under vis–NIR (Figure 6d). This indicates the stability and recyclability of the prepared composite. Moreover, the calculated

apparent quantum efficiency (AQE) of BTM1.5 at λ = 600 nm is 4.23%.

To understand the mechanism of CO<sub>2</sub> photoreduction into selective product(s) with a particular light source, certain vital points should be considered, such as the pathway of the charge carriers with regard to the light source and the band position of the accumulated charge carriers (DRS–UV–vis, Mott–Schottky, and VB–XPS have addressed the same). In situ irradiated XPS (ISI-XPS) was conducted to understand the feasible charge migration mechanism in the heterostructure<sup>[39,43,66,67]</sup>; and confirm the charge migration pathway is switchable from a type-II heterojunction system to an S-scheme system under selective light wavelength.

In the absence of light irradiation, Ti 2p<sub>3/2</sub>, Bi 4f<sub>7/2</sub>, and Mo 3d<sub>5/2</sub> peaks are respectively positioned at 459.05, 158.65, and 229.3 eV. Under UV light irradiation, Ti 2p binding energies showed a slight positive shift (by 0.45 eV) (Figure 7a), implying a decline in their electron density. This energy decrease confirms that the electron transition is from TiO<sub>2</sub> to either Bi<sub>2</sub>S<sub>3</sub> or MoS<sub>2</sub> during UV–vis–NIR light irradiation. In contrast, a negative shift (by −0.35 eV) during visible light irradiation is observed (Figure 7a), implying a rise in their electron density. The increase in the TiO<sub>2</sub> electron density during visible light irradiation confirms the transition of electrons from Bi<sub>2</sub>S<sub>3</sub> or MoS<sub>2</sub> to the conduction band of TiO<sub>2</sub>. Meanwhile, during UV–vis–NIR light irradiation, the Bi 4f and Mo 3d binding energies showed a negative shift by 0.35 and 0.5 eV, respectively, implying a rise in their

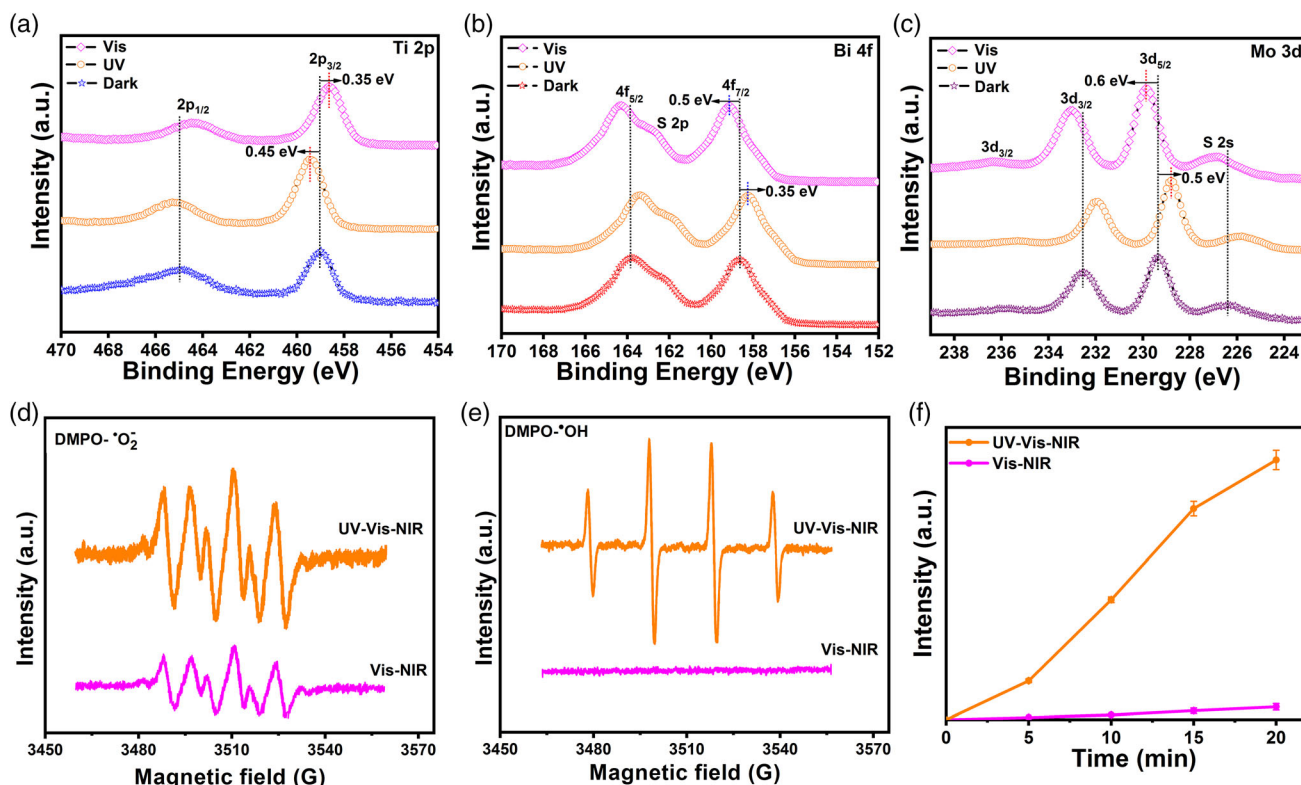


**Figure 7.** ISI-XPS of a) Ti 2p, b) Bi 4f, and c) Mo 3d; ESR spectra of BTM1.5 sample with DMPO obtained under both UV–vis–NIR and vis–NIR irradiation d) in aqueous suspension to detect DMPO–•OH species and e) in methanol to detect DMPO–•O<sub>2</sub><sup>−</sup> species; f) changes of the TA-PL spectra at 425 nm obtained by BTM1.5 sample under UV–vis–NIR and vis–NIR irradiation over time.



electron density and confirming the electron accumulation on their surfaces. This indicates that  $\text{Bi}_2\text{S}_3$  and  $\text{MoS}_2$  are the active sites under UV–vis–NIR irradiation.

Contrarily, under visible light irradiation, Bi 4*f* and Mo 3*d* binding energies showed positive shift by 0.5 and 0.6 eV, respectively (Figure 7b,c), indicating a decline in their electron density and confirming the transformation of electrons to the surface of  $\text{TiO}_2$ , implying that  $\text{TiO}_2$  is the active site under vis–NIR irradiation. Such binding energy transition under different light irradiations represents a clear picture of charge carriers' migration pathway across the  $\text{Bi}_2\text{S}_3/\text{TiO}_2/\text{MoS}_2$  interface. In particular, the transitions of excited electrons between  $\text{Bi}_2\text{S}_3$ ,  $\text{TiO}_2$ , and  $\text{MoS}_2$  are in excellent accordance with the S-scheme system under UV light irradiation and with the heterojunction system under visible light irradiation. Furthermore, from the positions of Bi 4*f*, Ti 2*p*, and Mo 3*d* binding energies without light irradiation, the Ti 2*p* binding energy experienced a positive shift,<sup>[68]</sup> whereas the Bi 4*f* and Mo 3*d* binding energies underwent a negative shift.<sup>[68]</sup> This observation indicates the strong interfacial interaction among  $\text{TiO}_2$ ,  $\text{MoS}_2$  and  $\text{Bi}_2\text{S}_3$ .<sup>[7,69]</sup>

To further verify the charge carrier migration in the  $\text{Bi}_2\text{S}_3/\text{TiO}_2/\text{MoS}_2$  heterostructure, spin-trapping electron spin resonance (ESR) analysis was performed in which the superoxide ( $\bullet\text{O}_2^-$ ) and hydroxyl ( $\bullet\text{OH}$ ) radicals were detected using 5,5-dimethyl pyrroline N-oxide (DMPO) as the free radical trapping agent in aqueous and methanol solution, respectively.<sup>[8,62]</sup> The ESR signals of BTM1.5 for  $\bullet\text{O}_2^-$  detection under UV–vis–NIR are shown in Figure 7d, where the signals show higher intensity than that under vis–NIR irradiation. This indicates more  $\bullet\text{O}_2^-$  is generated under UV–vis–NIR due to higher charge carrier separation and enhanced charge accumulation band potential position (S-scheme pathway). In contrast, for  $\bullet\text{OH}$  detection (Figure 7e), no peaks are observed under vis–NIR, whereas the characteristic peaks of DMPO– $\bullet\text{OH}$  strongly appear under UV–vis–NIR irradiation.

Thus, the production of  $\bullet\text{OH}$  under UV–vis–NIR indicates that the charge migration pathway follows the S-scheme approach, whereas under vis–NIR, the heterojunction system proceeds. However, the generation of  $\bullet\text{OH}$  was further investigated through terephthalic acid photoluminescence (TA-PL) technique (Figure 7f). No PL spectra of the TA solution in the presence of BTM1.5 was detected for the first 10 min of vis–NIR irradiation. Under UV–vis–NIR irradiation, PL spectra of the TA solution in the presence of BTM1.5 appeared, with the intensity increasing with irradiation time. This result confirms the ISI-XPS and ESR result of the charge migration pathway. Moreover, a radical scavenging experiment was conducted for RhB photodegradation under UV–vis–NIR and vis–NIR irradiation to further confirm the dominant radicals generated when the light wavelength range is changed. Figure S3a,b, Supporting Information, shows the photocatalytic reaction of BTM1.5 toward RhB dye degradation in the presence of BQ,  $\text{Na}_2\text{SO}_4$ , TBA, and KI, which are the scavenging materials for  $\bullet\text{O}_2^-$ , electrons,  $\bullet\text{OH}$ , and holes, respectively.<sup>[63,69–72]</sup> Under UV–vis–NIR, the charge carriers,  $\bullet\text{O}_2^-$  and  $\bullet\text{OH}$ , effectively contributed for the degradation of RhB, whereas under vis–NIR, only electrons and  $\bullet\text{O}_2^-$  were the major responses for the photocatalytic reaction. These results clearly demonstrate that under UV–vis–NIR, the

charge migration pathway follows the S-scheme system, and under vis–NIR, the heterojunction system is followed.

In principle, electron–hole pairs are initiated with irradiation energy equivalent to or higher than the photocatalyst's bandgap energy (Equation (6) and (7)). In our case,  $\text{Bi}_2\text{S}_3$  ( $E_g = 1.48$  eV),  $\text{TiO}_2$  ( $E_g = 3.21$  eV), and  $\text{MoS}_2$  ( $E_g = 1.46$  eV) are the heterostructure components.  $\text{TiO}_2$  has a large bandgap that restricts the catalyst from absorbing only UV light to achieve photoactivation, whereas  $\text{Bi}_2\text{S}_3$  and  $\text{MoS}_2$  have smaller bandgaps that facilitate the sample photoactive under visible irradiation. The production of  $\text{CH}_4$ ,  $\text{CO}$ ,  $\text{CH}_3\text{OH}$ , and  $\text{C}_2\text{H}_5\text{OH}$  is a multistep reaction. As per band theory, the selectivity of the products is related to the redox potentials at the conduction band. Therefore, the CB potential of the composite must be more negative compared with the gaseous  $\text{CO}_2$  products,  $\text{CH}_4$  (−0.24 V vs NHE),  $\text{CO}$  (−0.53 V vs NHE),  $\text{CH}_3\text{OH}$  (−0.38 V vs NHE), and  $\text{C}_2\text{H}_5\text{OH}$  (−0.33 V vs NHE).<sup>[5,6,20]</sup>

Based on the previous discussion, results, and analyses, photocatalytic  $\text{CO}_2$  reduction was proposed with two promised mechanisms, S-scheme and heterojunction systems. Under UV–vis–NIR irradiation, the electrons in the VB of  $\text{TiO}_2$ ,  $\text{Bi}_2\text{S}_3$ , and  $\text{MoS}_2$  are excited to the CB, and due to the generated internal built-in electric field from  $\text{TiO}_2$  to  $\text{Bi}_2\text{S}_3$  and  $\text{MoS}_2$ , the electrons in the  $\text{TiO}_2$  CB would transfer and recombine with the holes in the VB of  $\text{Bi}_2\text{S}_3$  and  $\text{MoS}_2$ , forming a double S-scheme junction (Figure 8a). This S-scheme configuration improved the separation of the charge carriers and the redox potential. Eventually, the photogenerated electrons would accumulate in the CB of  $\text{Bi}_2\text{S}_3$  and  $\text{MoS}_2$  CBs and interact with the ionized  $\text{CO}_2$  molecules to generate  $\text{CH}_3\text{OH}$  and  $\text{C}_2\text{H}_5\text{OH}$  with water vapor as the proton source ( $\text{H}^+$ ). Considering the redox potential, the CBM of  $\text{Bi}_2\text{S}_3$  and  $\text{MoS}_2$  are sufficient for  $\text{CO}_2/\text{CH}_3\text{OH}$  (−0.38 V) and  $\text{CO}_2/\text{C}_2\text{H}_5\text{OH}$  (−0.33 V) production (Equation (8) and (9)). The emission rate of  $\text{CH}_3\text{OH}$  is much greater than that of  $\text{C}_2\text{H}_5\text{OH}$  because the redox energy of  $\text{CH}_3\text{OH}$  is more well correlated with the  $\text{Bi}_2\text{S}_3$  conduction band energy than that for the  $\text{C}_2\text{H}_5\text{OH}$ .<sup>[5]</sup> Moreover, the production of  $\text{CH}_3\text{OH}$  through  $\text{CO}_2$  adsorption involves  $6\text{H}^+$  paired with  $6\text{e}^-$ , while the production of  $\text{C}_2\text{H}_5\text{OH}$  through  $\text{CO}_2$  adsorption involves  $12\text{H}^+$  paired with  $12\text{e}^-$ . Consequently, the transformations are also in line with  $\text{CH}_3\text{OH}$  emission.

In contrast, in the photoreaction with vis–NIR irradiation, the electrons in the VB of  $\text{Bi}_2\text{S}_3$  and  $\text{MoS}_2$  can be excited to their CB, and  $\text{TiO}_2$  works as an electron acceptor (due to the large bandgap). In other words, as the position of the  $\text{TiO}_2$  CB is lower than that of  $\text{MoS}_2$  and  $\text{Bi}_2\text{S}_3$ , the electrons on the CB of  $\text{Bi}_2\text{S}_3$  and  $\text{MoS}_2$  will transfer and accumulate to the CB of  $\text{TiO}_2$ , forming type-II heterojunctions between  $\text{TiO}_2/\text{Bi}_2\text{S}_3$  and  $\text{TiO}_2/\text{MoS}_2$  (Figure 8b). Ultimately, the accumulated photogenerated electrons upon the  $\text{TiO}_2$  CB would interact with the ionized  $\text{CO}_2$  molecules to generate  $\text{CH}_4$  and  $\text{CO}$  with water as the source of the  $\text{H}^+$ . As per the redox potential scale, the CBM of  $\text{TiO}_2$  is −0.3 V, which is appropriate for  $\text{CO}_2/\text{CH}_4$  (−0.24 V) reaction (Equation (10)) but not for  $\text{CO}_2/\text{CO}$  (−0.53 V) reaction (Equation (11)).

However, the XPS study showed the development of reactive oxygen vacancy ( $\text{V}_\text{O}$ )/ $\text{Ti}^{3+}$  sites on the surface of BTM1.5. These defects would easily include an active reactant (electrical conductivity), leading to efficient electron or hole transfer between  $\text{CO}_2/$

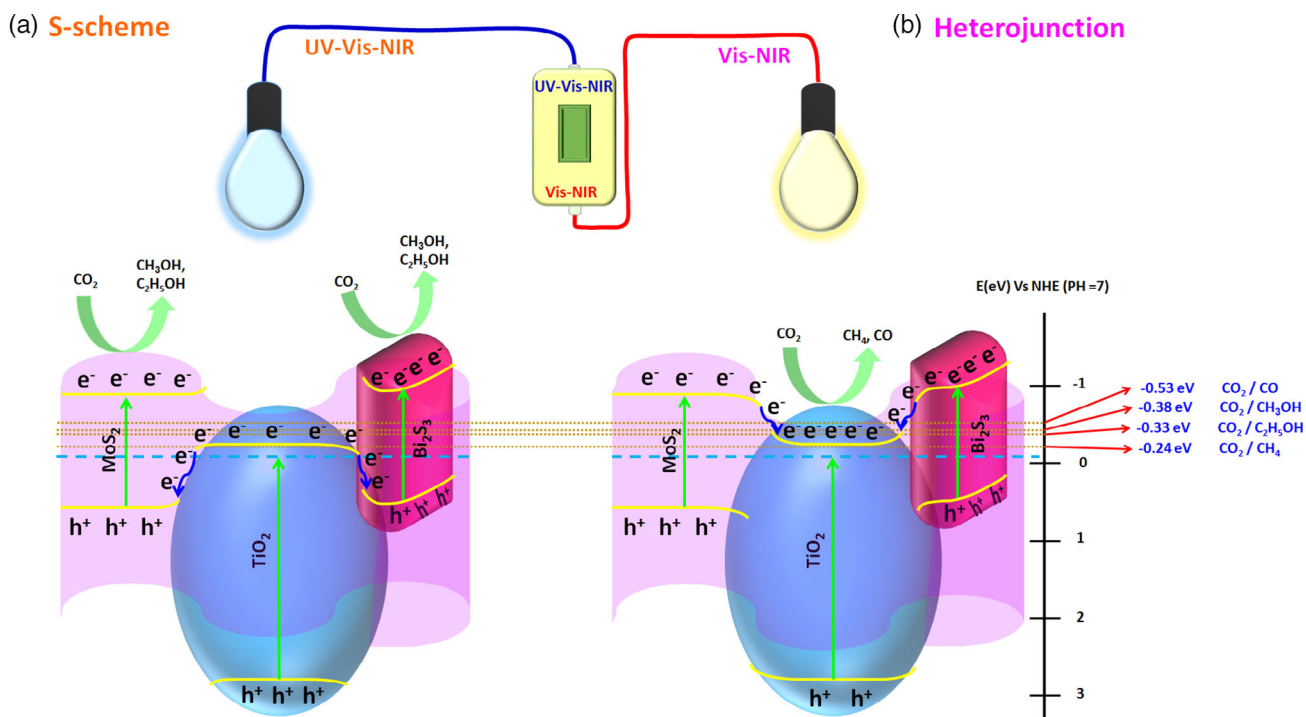
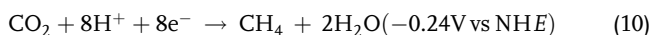
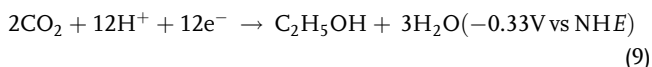
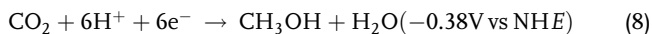
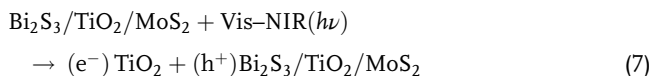
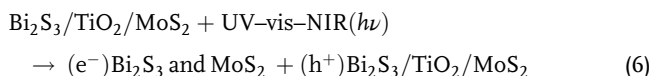


**Figure 8.** Proposed mechanism of CO<sub>2</sub> reduction a) under UV-vis-NIR and b) vis-NIR irradiation.

H<sub>2</sub>O and the irradiated TiO<sub>2-x</sub> surface.<sup>[15]</sup> Thus, the formation of CO is shown by Equation (12)–(17), starting with H<sub>2</sub>O dissociation (Equation (12)) and intermediate production (CO<sub>2</sub><sup>-</sup>, HCO<sub>3</sub><sup>-</sup>) on the surface of TiO<sub>2</sub> (Equation (13) and (14)).<sup>[15,73–75]</sup> CO<sub>2</sub><sup>-</sup> can be converted to CO via reaction with H<sup>+</sup> (Equation (15)) or self-recombination (Equation (16)) or immediate deactivation by the restoration of V<sub>O</sub> sites (Equation (17)). Moreover, the abundance of Ti<sup>3+</sup> plays an important role in the production and selectivity of CH<sub>4</sub>,<sup>[76]</sup> which might be the reason for the higher production of CH<sub>4</sub> over CO.



In summary, the electrons' flow direction strongly affects the photocatalytic activity of the heterostructure. The prepared composite showed switchable electron flow and improved redox potential with respect to a wavelength range of light. This selective redox potential resulted in the desired CO<sub>2</sub> reduction product.

### 3. Conclusion

A multidimensional Bi<sub>2</sub>S<sub>3</sub>/TiO<sub>2</sub>/MoS<sub>2</sub> heterostructure was prepared via a microwave hydrothermal method and used for photocatalytic CO<sub>2</sub> reduction. XRD and XPS results confirmed the structure formation. FE-SEM and TEM exhibit that the heterostructure is built up with excellent interfacial contact, where the TiO<sub>2</sub> nanosphere and Bi<sub>2</sub>S<sub>3</sub> nanorods were wrapped and embedded within the MoS<sub>2</sub> nanosheets. DRS-UV showed that the heterostructure is responsive to the entire spectrum of radiation. ISI-XPS analysis proved that the electrons' flow direction could be switched by varying the light wavelength range. Under UV-vis-NIR, the electrons tend to transfer from TiO<sub>2</sub> to MoS<sub>2</sub> and Bi<sub>2</sub>S<sub>3</sub>, forming an S-scheme heterojunction, whereas under vis-NIR, the electrons tend to transfer from Bi<sub>2</sub>S<sub>3</sub> and MoS<sub>2</sub> to TiO<sub>2</sub>, forming a type-II heterojunction, which is further supported by the ESR, TA-PL, and scavenger

experiments. As a result, changing the wavelength of the applied light changed the composite junction, leading to a switch in the redox potential of the accumulated charge carriers. The designed  $\text{Bi}_2\text{S}_3/\text{TiO}_2/\text{MoS}_2$  heterostructure exhibited selective photocatalytic  $\text{CO}_2$  reduction ( $\text{CH}_3\text{OH}$  and  $\text{C}_2\text{H}_5\text{OH}$  under UV–vis–NIR and  $\text{CH}_4$  and  $\text{CO}$  under vis–NIR). Interestingly, the quantum efficiency of the composite is 4.23% at 600 nm wavelength. These findings showed that tuning the photoinduced charge transport pathway and developing a direct S-scheme and/or type-II heterojunction may be done by selecting optimal heterostructure responses to different frequencies, which would improve the  $\text{CO}_2$  reduction selectivity.

## 4. Experimental Section

**Reagents:** Anatase  $\text{TiO}_2$  nanoparticles (>99%), bismuth nitrate pentahydrate (>98%), and sodium molybdate dehydrate (>99%) were purchased from Sigma-Aldrich. Sodium hydroxide ( $\geq 98\%$ ), hydrochloric acid (37%), sodium bicarbonate (98%), thiourea (99%), and acetone (>99.5) were purchased from Alfa Aesar. All the reagents were used with no further purification. Nanopure water was used for all the experiments.

**Synthesis of  $\text{TiO}_2/\text{Bi}_2\text{S}_3/\text{MoS}_2$ :** The heterostructure was prepared similarly to a previous report;<sup>[7]</sup> however, commercial anatase  $\text{TiO}_2$  nanoparticles was used and the molar ratio of  $\text{MoS}_2$  instead of  $\text{TiO}_2$  was varied. Typically, 2.7 g of  $\text{Bi}(\text{NO}_3)_3 \cdot 5\text{H}_2\text{O}$  and 5.4 g of thiourea were dissolved in 90 mL of water (labeled as S1). More suspension was made by sonicating 1.8 g of anatase  $\text{TiO}_2$  nanoparticles in 90 mL of water for 3 min (labeled as S2). Another suspension was prepared by dissolving 1.8 g of sodium molybdate dihydrate and 5.4 g of thiourea in 60 mL of water (labeled as S3). Ten milliliters from S1 and S2 each was added into five different Teflon vessels with different volumes (2.5, 5, 10, 15, and 20 mL) of S3. The samples were labeled as BTM-0.25, BTM-0.5, BTM-1, BTM-1.5, and BTM-2, respectively. Similarly, BTM-0 was prepared without the addition of S3. An appropriate amount of water was applied to each Teflon vessel to sustain 40 mL of the total volume of the solution. Other pristine photocatalysts,  $\text{Bi}_2\text{S}_3$  and  $\text{MoS}_2$ , were synthesized using S1 and S3 solutions for the photocatalytic efficiency comparison. The solutions were eventually moved to a microwave reaction system (Anton-Paar Multiwave PRO). Microwave heating conditions were as follows: heating temperature = 200 °C, heating time = 30 min, pressure =  $\approx 80$  bar, holding reaction time = 60 min, and cooling time = 60 min. The substance was centrifuged after the reaction and washed with absolute ethanol and distilled water. Finally, the samples were dried for 12 h in a hot-air oven at 60 °C.

**Analytical Methods:** A Rigaku diffractometer investigated the crystallites of the samples, equipped with a  $\text{Cu K}\alpha$  radiation source ( $\lambda = 1.5406 \text{ \AA}$ ). The prepared samples' morphology was examined using FE-SEM (TESCAN Lyras 3) and HR-TEM (Joel/JEM 2100 model). The elemental analysis was approved using XPS (ESCALAB 250Xi, Thermo Scientific). Optical properties were investigated using UV–vis DRS (Shimadzu UV-3600 UV) and PL (Hitachi, F-2700) spectrophotometers. BET surface area (Micromeritics Tristar II Plus analyzer) was measured by  $\text{N}_2$  adsorption; UPS was used to obtain the work function and VB potential.

**Photocatalytic  $\text{CO}_2$  Reduction:** The efficiency of the synthesized photocatalysts was examined toward  $\text{CO}_2$  reduction at room temperature upon 300 W xenon lamp (UV–vis–NIR = 200–1200 nm) and (vis–NIR = 400–1200 nm). In a 150 mL quartz reactor (Scheme S1, Supporting Information), 50 mg of the selected sample was dispersed in 10 mL nanopure water and sonicated for 30 min, then placed in a hot air oven at 70 °C for 10 h, resulting in a thin film at the bottom of the reactor. The reactor was then loaded with 0.12 g of  $\text{NaHCO}_3$ , sealed with a rubber septum, and purified with Ar gas for 30 min prior to the illumination to achieve anaerobic conditions.  $\text{CO}_2$  gas and  $\text{H}_2\text{O}$  vapor were in situ produced by injection of 0.35 M HCl aqueous solution. A GC-2014C Shimadzu gas chromatograph equipped with a flame ionization detector (FID) and a methanizer were used to detect the mixed gas (250  $\mu\text{L}$ ) withdrawn from the reactor

after an hour's irradiation. The stability test and recyclability test of the optimized sample were recorded after 4 h of photoreaction. To quantify the AQE, the photoreaction of all BTM samples was performed at 600 nm bandpass filter, and Equation (18) calculated the photocatalytic products.

$$\text{AQE} = [N_p (\text{mol s}^{-1}) / N_{ph} (\text{mol s}^{-1})] \times 100 \quad (18)$$

$N_p$  = number of reductions in the electron  $\times$  moles of product yield ( $\text{mol s}^{-1}$ ), and  $N_{ph}$  denotes moles of photon flux ( $\text{mol s}^{-1}$ ).  $N_{ph}$  was calculated using Equation (19).

$$N_{ph} = I (\text{W m}^{-2}) \times A (\text{m}^2) \times t / [(hc/\lambda) \times N_A] \quad (19)$$

where  $I$  is the intensity of incident light,  $A$  is the light illumination area,  $t$  is the illumination time,  $h$  is Planck's constant,  $c$  is the speed of light, and  $N_A$  is Avogadro's constant ( $6.022 \times 10^{23} \text{ mol}^{-1}$ ).

**Electrochemical Measurements:** A CHI 608e electrochemical analyzer was used to determine the photocurrent densities of the synthesized samples. The working electrode was made of fluorine-doped tin oxide (FTO) glass spin coated with the examined sample. Platinum wire and Ag/AgCl electrodes were used as reference and counter electrodes, respectively, and  $\text{Na}_2\text{SO}_4$  (0.5 M) was used as an electrolyte. Before immersing the three electrodes in the electrolyte,  $\text{Na}_2\text{SO}_4$  was purged with argon for 0.5 h. A 150 W xenon lamp was used to irradiate the working electrode at 50  $\text{mW cm}^{-2}$ , and the current density was recorded at 0 V during light off–on cycling.

**In situ Irradiated X-ray Photoelectron Spectroscopy:** The chemical composition and the corresponding states of the BTM1.5 sample were investigated by XPS using a Thermo Scientific (ESCALAB 250Xi) instrument. To explore the electron density changes caused by light irradiation, an ISI-XPS investigation was performed using the same instrument supplied with a low-power 365 nm UV lamp and 600 nm visible lamp as light source illumination (Shenzhen LAMPLIC Science Co. Ltd., China).

**Spin-Trapping Electron Spin Resonance:** To confirm the switchability of the charge carrier's migration pathway, ESR was utilized to determine the  $\cdot\text{O}_2^-$  and  $\cdot\text{OH}$  by incorporating DMPO as the reactive species scavenging agent in methanol and aqueous solutions, respectively. At room temperature, 5 mg of BTM1.5 was sonicated for 10 min in 1 mL water/methanol and 50 mL DMPO. The signals were recorded on a JES FA200 spectrometer upon UV–vis–NIR and vis–NIR illumination.

**Terephthalic Acid Photoluminescence:** The generation of  $\cdot\text{OH}$  during UV–vis–NIR and vis–NIR irradiation upon BTM1.5 was further confirmed using the TA-PL technique. 30 mM of terephthalic acid was used to trap the generated  $\cdot\text{OH}$  during UV–vis–NIR or vis–NIR illumination, which resulted in 2-hydroxy terephthalic acid detection under a PL spectrometer at fluorescence peak position around 425 nm, which was increasing over the time of irradiation.

## Supporting Information

Supporting Information is available from the Wiley Online Library or from the author.

## Acknowledgements

The authors are thankful to the DST National Single Crystal Diffractometer Facility Laboratory, DoS in Physics, UPE, IOE, and DST-PURSE, Vijnana Bhavana, University of Mysore, Mysuru, for providing the required facilities. The authors extend their appreciation to the Researchers Supporting Project number (RSP-2021/381), King Saud University, Riyadh, Saudi Arabia.

## Conflict of Interest

The authors declare no conflict of interest.

## Data Availability Statement

Research data are not shared.

## Keywords

Bi<sub>2</sub>S<sub>3</sub>/TiO<sub>2</sub>/MoS<sub>2</sub> heterostructures, CO<sub>2</sub> reduction, product selectivity, electron flow regulation, redox potential switchability

Received: July 5, 2021

Revised: August 16, 2021

Published online:

- [1] L. Al-Ghussain, *Environ. Prog. Sustainable Energy* **2019**, 38, 13.
- [2] X. Zhang, F. Han, B. Shi, S. Farsinezhad, G. P. Dechaine, K. Shankar, *Angew. Chem. Int. Ed.* **2012**, 51, 12732.
- [3] T. Wu, L. Zou, D. Han, F. Li, Q. Zhang, L. Niu, *Green Chem.* **2014**, 16, 2142.
- [4] N. Shehzad, M. Tahir, K. Johari, T. Murugesan, M. Hussain, J. CO<sub>2</sub> Util. **2018**, 26, 98.
- [5] S. Ijaz, M. F. Ehsan, M. N. Ashiq, T. He, *Catal. Sci. Technol.* **2015**, 5, 5208.
- [6] K. Li, B. Peng, T. Peng, *ACS Catal.* **2016**, 6, 7485.
- [7] Q. Drmash, A. Hezam, A. Hendi, M. Qamar, Z. Yamani, K. Byrappa, *Appl. Surf. Sci.* **2020**, 499, 143938.
- [8] C. K. Swamy, A. Hezam, A. M. Ramesh, D. H. Ramakrishnegowda, D. K. Purushothama, J. Krishnegowda, S. Shivanna, *J. Photochem. Photobiol. A* **2021**, 418, 113394.
- [9] F. Ye, Y. Su, X. Quan, S. Chen, H. Yu, H. Li, *Appl. Catal. B* **2019**, 244, 347.
- [10] Y. Zhang, B. Xia, J. Ran, K. Davey, S. Z. Qiao, *Adv. Energy Mater.* **2020**, 10, 1903879.
- [11] C. Ji, C. Liang, Q. Song, H. Gong, N. Liu, F. You, D. Li, Z. He, *Sol. RRL* **2021**, 5, 2100072.
- [12] J. Ran, M. Jaroniec, S. Z. Qiao, *Adv. Mater.* **2018**, 30, 1704649.
- [13] J. Wang, S. Lin, N. Tian, T. Ma, Y. Zhang, H. Huang, *Adv. Funct. Mater.* **2020**, 31, 2008008.
- [14] Y. Y. Lee, H. S. Jung, Y. T. Kang, J. CO<sub>2</sub> Util. **2017**, 20, 163.
- [15] L. Liu, H. Zhao, J. M. Andino, Y. Li, *ACS Catal.* **2012**, 2, 1817.
- [16] N. Murakami, D. Saruwatari, T. Tsubota, T. Ohno, *Curr. Org. Chem.* **2013**, 17, 2449.
- [17] J. Low, B. Cheng, J. Yu, *Appl. Surf. Sci.* **2017**, 392, 658.
- [18] J. Fu, S. Cao, J. Yu, J. Low, Y. Lei, *Dalton Trans.* **2014**, 43, 9158.
- [19] Q. Xu, J. Yu, J. Zhang, J. Zhang, G. Liu, *Chem. Commun.* **2015**, 51, 7950.
- [20] O. Ola, M. M. Maroto-Valer, *J. Photochem. Photobiol. C* **2015**, 24, 16.
- [21] T. P. Nguyen, D. L. T. Nguyen, V. H. Nguyen, T. H. Le, D. N. Vo, Q. T. Trinh, S. R. Bae, S. Y. Chae, S. Y. Kim, Q. V. Le, *Nanomaterials* **2020**, 10, 337.
- [22] R. Kim, J. Kim, J. Y. Do, M. W. Seo, M. Kang, *Catalysts* **2019**, 9, 998.
- [23] S. Sun, Q. An, M. Watanabe, J. Cheng, H. H. Kim, T. Akbay, A. Takagaki, T. Ishihara, *Appl. Catal. B* **2020**, 271, 118931.
- [24] F. Xu, B. Zhu, B. Cheng, J. Yu, J. Xu, *Adv. Opt. Mater.* **2018**, 6, 1800911.
- [25] X. Li, H. Liu, D. Luo, J. Li, Y. Huang, H. Li, Y. Fang, Y. Xu, L. Zhu, *Chem. Eng. J.* **2012**, 180, 151.
- [26] Q. Xiang, J. Yu, M. Jaroniec, *J. Am. Chem. Soc.* **2012**, 134, 6575.
- [27] S. Sadhasivam, N. Anbarasan, M. Mukilan, P. Manivel, K. Jeganathan, *Int. J. Hydrogen Energy* **2020**, 45, 30080.
- [28] Y. Liu, Y. Li, F. Peng, Y. Lin, S. Yang, S. Zhang, H. Wang, Y. Cao, H. Yu, *Appl. Catal. B* **2019**, 241, 236.
- [29] C. García-Mendoza, S. Oros-Ruiz, A. Hernández-Gordillo, R. López, G. Jácome-Acatitla, H. A. Calderón, R. Gómez, *J. Chem. Technol. Biotechnol.* **2016**, 91, 2198.
- [30] Y. Zhou, Z. Wang, L. Huang, S. Zaman, K. Lei, T. Yue, Z. A. Li, B. You, B. Y. Xia, *Adv. Energy Mater.* **2021**, 11, 2003159.
- [31] J. Fu, Q. Xu, J. Low, C. Jiang, J. Yu, *Appl. Catal. B* **2019**, 243, 556.
- [32] H. B. Lee, N. Kumar, B. Tyagi, K.-J. Ko, J. W. Kang, *Sol. RRL* **2021**, 5, 2000589.
- [33] K. Li, T. Peng, Z. Ying, S. Song, J. Zhang, *Appl. Catal. B* **2016**, 180, 130.
- [34] M. Tahir, B. Tahir, N. A. S. Amin, H. Alias, *Appl. Surf. Sci.* **2016**, 389, 46.
- [35] W. Jiang, X. Zong, L. An, S. Hua, X. Miao, S. Luan, Y. Wen, F. F. Tao, Z. Sun, *ACS Catal.* **2018**, 8, 2209.
- [36] J. Zhang, D. Zhou, S. Dong, N. Ren, *J. Hazard. Mater.* **2019**, 366, 311.
- [37] F. Xu, K. Meng, B. Cheng, S. Wang, J. Xu, J. Yu, *Nat. Commun.* **2020**, 11, 4613.
- [38] Q. Xu, L. Zhang, B. Cheng, J. Fan, J. Yu, *Chem* **2020**, 6, 1543.
- [39] S. Wu, X. Yu, J. Zhang, Y. Zhang, Y. Zhu, M. Zhu, *Chem. Eng. J.* **2021**, 411, 128555.
- [40] H. Deng, X. Fei, Y. Yang, J. Fan, J. Yu, B. Cheng, L. Zhang, *Chem. Eng. J.* **2021**, 409, 127377.
- [41] O. S. Ekande, M. Kumar, *J. Environ. Chem. Eng.* **2021**, 9, 105725.
- [42] X. Liu, C. Bie, B. He, B. Zhu, L. Zhang, B. Cheng, *Appl. Surf. Sci.* **2021**, 554, 149622.
- [43] H. Ge, F. Xu, B. Cheng, J. Yu, W. Ho, *ChemCatChem* **2019**, 11, 6301.
- [44] J. Wang, G. Wang, B. Cheng, J. Yu, J. Fan, *Chin. J. Catal.* **2021**, 42, 56.
- [45] C. H. Wang, D. D. Qin, D. L. Shan, J. Gu, Y. Yan, J. Chen, Q. H. Wang, C. H. He, Y. Li, J. J. Quan, X. Q. Lu, *Phys. Chem. Chem. Phys.* **2017**, 19, 4507.
- [46] N. Nie, L. Zhang, J. Fu, B. Cheng, J. Yu, *Appl. Surf. Sci.* **2018**, 441, 12.
- [47] Y. X. Zeng, X. W. Zhong, Z. Q. Liu, S. Chen, N. Li, *J. Nanomater.* **2013**, 2013, 1.
- [48] B. Bharti, S. Kumar, H.-N. Lee, R. Kumar, *Sci. Rep.* **2016**, 6, 32355.
- [49] B. Li, L. Jiang, X. Li, P. Ran, P. Zuo, A. Wang, L. Qu, Y. Zhao, Z. Cheng, Y. Lu, *Sci. Rep.* **2017**, 7, 11182.
- [50] Z. Wu, B. Fang, Z. Wang, C. Wang, Z. Liu, F. Liu, W. Wang, A. Alfantazi, D. Wang, D. P. Wilkinson, *ACS Catal.* **2013**, 3, 2101.
- [51] R. Li, W. Zhang, K. Zhou, *Adv. Mater.* **2018**, 30, 1705512.
- [52] E. Pineda, M. E. Nicho, P. Nair, H. Hu, *Sol. Energy* **2012**, 86, 1017.
- [53] Y. Huang, P. Wang, Z. Wang, Y. Rao, J. J. Cao, S. Pu, W. Ho, S. C. Lee, *Appl. Catal. B* **2019**, 240, 122.
- [54] D. Barpuzary, A. Banik, G. Gogoi, M. Qureshi, *J. Mater. Chem. A* **2015**, 3, 14378.
- [55] N. Mahuli, D. Saha, S. K. Sarkar, *J. Phys. Chem. C* **2017**, 121, 8136.
- [56] M. Guo, T. Zhao, Z. Xing, Y. Qiu, K. Pan, Z. Li, S. Yang, W. Zhou, *ACS Appl. Mater. Interfaces* **2020**, 12, 40328.
- [57] S. Chuang, C. Battaglia, A. Azcatl, S. McDonnell, J. S. Kang, X. Yin, M. Tosun, R. Kapadia, H. Fang, R. M. Wallace, *Nano Lett.* **2014**, 14, 1337.
- [58] F. Xue, L. Chen, J. Chen, J. Liu, L. Wang, M. Chen, Y. Pang, X. Yang, G. Gao, J. Zhai, *Adv. Mater.* **2016**, 28, 3391.
- [59] S. Hua, D. Qu, L. An, W. Jiang, Y. Wen, X. Wang, Z. Sun, *Appl. Catal. B* **2019**, 240, 253.
- [60] G. Shao, *Energy Environ. Mater.* **2021**, 4, 1.
- [61] J. Li, Z. Li, X. Liu, C. Li, Y. Zheng, K. W. K. Yeung, Z. Cui, Y. Liang, S. Zhu, W. Hu, *Nat. Commun.* **2021**, 12, 529.



- [62] S. A. Mahyoub, A. Hezam, F. A. Qaraah, K. Namratha, M. B. Nayan, Q. A. Drmsh, D. Ponnamma, K. Byrappa, *ACS Appl. Energy Mater.* **2021**, 4, 3544.
- [63] K. Alkanad, A. Hezam, G. C. Sujay Shekar, Q. A. Drmsh, A. A. Kala, M. Q. AL-Gunaid, N. K. Lokanath, *Catal. Sci. Technol.* **2021**, 11, 3084.
- [64] F. He, B. Zhu, B. Cheng, J. Yu, W. Ho, W. Macyk, *Appl. Catal. B* **2020**, 272, 119006.
- [65] A. Hezam, K. Namratha, D. Ponnamma, A. M. N. Saeed, V. Ganesh, B. Neppolian, K. Byrappa, *J. Mater. Chem. A* **2018**, 6, 21379.
- [66] A. Hezam, J. Wang, Q. Drmsh, P. Karthik, M. A. Bajiri, K. Namratha, M. Zare, T. Lakshmeesha, S. Shivanna, C. Cheng, *Appl. Surf. Sci.* **2020**, 451, 148457.
- [67] J. Low, B. Dai, T. Tong, C. Jiang, J. Yu, *Adv. Mater.* **2019**, 31, 1802981.
- [68] J. F. Moulder, J. Chastain, R. C. King, *Handbook of X-Ray Photoelectron Spectroscopy: A Reference Book of Standard Spectra for Identification and Interpretation of XPS Data*, Physical Electronics, Perkin-Elmer Corp, Eden Prairie, MN, USA **1995**.
- [69] A. Hezam, K. Namratha, D. Ponnamma, Q. Drmsh, A. M. N. Saeed, C. Cheng, K. Byrappa, *ACS Omega* **2018**, 3, 12260.
- [70] G. C. Sujay Shekar, K. Alkanad, A. Hezam, A. Alsalme, N. Al-Zaqri, N. K. Lokanath, *J. Mol. Liq.* **2021**, 335, 116186.
- [71] N. Denisov, J. Yoo, P. Schmuki, *Electrochim. Acta* **2019**, 319, 61.
- [72] M. A. Bajiri, A. Hezam, N. Keerthiraj, B. M. Al-Maswari, H. S. B. Naik, K. Byrappa, N. A. Zaqri, A. Alsalme, R. Alasmari, *New J. Chem.* **2021**, 45, 13499.
- [73] J. Lee, D. C. Sorescu, X. Deng, *J. Am. Chem. Soc.* **2011**, 133, 10066.
- [74] N. M. Dimitrijevic, B. K. Vijayan, O. G. Poluektov, T. Rajh, K. A. Gray, H. He, P. Zapol, *J. Am. Chem. Soc.* **2011**, 133, 3964.
- [75] W. Pipornpong, R. Wanbayor, V. Ruangpornvisuti, *Appl. Surf. Sci.* **2011**, 257, 10322.
- [76] Z. W. Wang, Q. Wan, Y. Z. Shi, H. Wang, Y. Y. Kang, S. Y. Zhu, S. Lin, L. Wu, *Appl. Catal. B* **2021**, 288, 120000.